Title
Quantification of 89Zr-Iron oxide nanoparticle biodistribution using PET-MR and ultrashort TE sequences

Permalink

Journal

ISSN

Authors
Jordan, Caroline D
Han, Misung
Kondapavulur, Sravani
et al.

Publication Date

DOI

Peer reviewed

Quantification of 89Zr-Iron Oxide Nanoparticle Biodistribution Using PET-MR and Ultrashort TE Sequences

Caroline D. Jordan, PhD[1], **Misung Han, PhD**[1], **Sravani Kondapavulur, BS**[1,2], **Denis Beckford Vera, PhD**[1], **Kiel D. Neumann, PhD**[1], **Teri Moore, BS, RT**[1], **Carol Stillson, RVT**[1], **Roland Krug, PhD**[1], **Spencer Behr, MD**[1], **Youngho Seo, PhD**[1], **Henry F. VanBrocklin, PhD**[1], **Peder E. Z. Larson, PhD**[1], **Mark Wilson, MD**[1], **Alastair J. Martin, PhD**[1], and **Steven W. Hetts, MD**[1]

[1]Department of Radiology and Biomedical Imaging, University of California San Francisco, San Francisco, CA, USA

[2]Department of Bioengineering and Therapeutic Sciences, University of California Berkeley, Berkeley, CA, USA

INTRODUCTION

One developing application of magnetic nanoparticles is to use magnetically linked drugs in intra-arterial chemotherapy (IAC) procedures (1). These magnetic drugs can then be selectively removed by deploying an endovascular magnetic device downstream of the targeted organ (1, 2), thus limiting off-target drug toxicities. *In vitro* studies used radiolabeled iron oxide nanoparticles (IONP) to quantify the number of particles captured on the device using a gamma counter (2). To demonstrate efficacy *in vivo*, accurate quantification of the drug's distribution on the device, within the targeted organ, and systemically, is necessary. The purpose of this study is to validate PET/MRI image-based quantification, using ^{89}Zr-PET signal, transverse relaxation rate (R_2^*), and quantitative magnetic susceptibility (χ) of ferromagnetic ^{89}Zr-IONP biodistribution *in vitro* and *in vivo*.

METHODS

In vitro experiment

Iron oxide (Fe_3O_4) nanoparticles with 50–100 nm diameter were used (Sigma-Aldrich, St. Louis, MO). Zirconium-89 (1.01 mCi, 2 μL) in 1M oxalic acid (3D imaging, Little Rock, AK) was added to IONPs (16.75 mg, 200 μL) in deionized (DI) water and 2 μL of 1M Na_2CO_3. The mixture was heated at 120˚C for 2 hours, and the ^{89}Zr-IONPs were purified using a magnet. A phantom was constructed using a cylinder of gelatin with five embedded plastic spheres with increasing ^{89}Zr-IONP concentrations of [2.5, 5, 10, 20, 30] mg/L. We used a 3.0T PET/MR (SIGNA, GE Healthcare, Waukesha, WI), with a head and neck coil with 12 channels for simultaneous acquisition of a 10-minute time-of-flight (TOF) static PET and MR data. A 3D multi-echo gradient echo UTE research sequence with a cones *k*-space trajectory (3) was used with TE = [0.148, 3.3, 5.6, 7.9] ms, TR = 13.2 ms, flip angle

Corresponding Author and Reprint Info: Steven W. Hetts, MD, steven.hetts@ucsf.edu, Department of Radiology and Biomedical Imaging, University of California San Francisco, 185 Berry Street, Suite 350, San Francisco, CA 94143.

12°, matrix 128×128, slice thickness 3 mm, field of view (FOV) 16×16 cm^2, a coronal scan plane, a fat-suppression pulse applied every five TRs, and slab-selection.

In vivo experiment

With Institutional Animal Care and Use Committee approval, a 5 French catheter (Slip-Cath® Beacon® Tip, Cook Medical, Bloomington, IN) was placed into the common hepatic artery of a supine swine (45.8 kg, female), using X-ray guidance (Cios Alpha, Siemens Healthineers, Munich, Germany). Radiolabeling was the same as before, using 3.05 mCi ^{89}Zr per 25 mg IONPs in 10 ml saline, shaken and separated into three aliquots: 1, 4, and 5 ml. We imaged before infusion, moved the scanner table away from the magnet bore for infusion, then imaged after each infusion. We used the same sequences as the *in vitro* study, except with an axial scan plane, 10 mm slice thickness, TE = [0.148 1.8, 3.6, 5.4] ms, TR = 10.2 ms, FOV 26×26 cm^2, and an 18-channel upper anterior array coil and posterior array to acquire a breath-held sequence.

Data analysis

PET images were reconstructed using a TOF ordered subsets expectation maximization algorithm in a 256×256 matrix, 5 iterations, 28 subsets, point-spread-function model, and a standard z-axis post filter with cutoff 3.0 mm full-width at half maximum. We used non-attenuation correction (NAC) images *in vitro*, and attenuation-corrected (AC) images *in vivo*. Regions of interest (ROI) were manually drawn on an MR image slice (OsiriX v.6.0.2, Pixmeo SARL, Geneva, Switzerland). Post-processing was performed in MATLAB 2016a (MathWorks Inc., Natick, MA). PET ROIs were interpolated to match the MR resolution for pixel-wise analysis. R_2* was measured using a mono-exponential fit of magnitude images. Quantitative susceptibility maps (QSM) were reconstructed using the Morphology Enabled Dipole Inversion (MEDI) toolbox (4–7). *In vitro*, we used a spherical mean value operator of radius 5, a regularization parameter of $\lambda = 10^{1.25}$, a scaling factor of 2.5303 and a global shift of −0.2554 ppm. *In vivo*, the same values were used, except using no scaling, $\lambda = 10^4$ pre-infusion, and $\lambda = 10^{2.5}$ post-infusion. A linear regression model was performed for the mean of each parameter ROI and IONP concentration, and then pixel-wise between each contrast mechanism.

RESULTS

In vitro results

There was a significant linear relationship with good correlation between ^{89}Zr-IONP concentration and the mean for each parameter (Fig. 1, Table 1). Each parameter also demonstrated a significant linear relationship with each other pixel-wise, which was well described by the least-squares fit line (Fig. 1c).

In vivo results

Mean ^{89}Zr-PET, R_2*, and χ showed good correlation with a linear relationship to concentration, but only R_2* demonstrated significance (Fig. 2, Table 2). ^{89}Zr-PET and R_2* showed the best correlation with each other, and lower correlations were shown between χ and R_2* and χ and ^{89}Zr-PET (Fig. 2e).

DISCUSSION

All three parameters, ^{89}Zr-PET, R$_2$*, and χ, had a significant linear relationship with ^{89}Zr-IONP concentration *in vitro*, which were well explained by the least-squares fit equations. ^{89}Zr-PET and R$_2$* had the highest correlations with ^{89}Zr-IONP concentration, followed by χ. ^{89}Zr-PET and R$_2$* had the best correlation with each other, then χ and ^{89}Zr-PET, and then χ and R$_2$*. *In vivo*, there was a significant linear relationship between the ^{89}Zr-IONP concentration and R$_2$*, but not χ or ^{89}Zr-PET. *In vivo*, ^{89}Zr-PET and R$_2$* had the best correlation with each other, whereas χ and R$_2$*, and χ and ^{89}Zr-PET had lower correlation coefficients.

While this paper includes validation in a phantom and feasibility *in vivo*, this study has limitations. The liver has unique challenges that affect QSM accuracy, including chemical shift caused by fat. A water-fat separation method would provide more accuracy (8). Fat-saturation appeared slightly inhomogeneous. It may also suppress some water signal, leading to lowered SNR and R$_2$* estimates (9), so our R$_2$* rates may be low.   R$_2$* may be required for broader ranges. It was difficult to achieve a homogenous IONP distribution in the phantom and liver. The nanoparticles are used as a proxy for magnetically linked drugs; the drug delivery mechanism needs to be optimized for hepatic delivery, since malignant liver tumors do not uptake superparamagnetic iron oxides (10). Since the endovascular filtration device is magnetic, it cannot be used in the scanner, and PET/MRI quantification cannot be performed real-time during the infusion; co-registration between scans will be needed.

In conclusion, this study demonstrated feasibility of image-based quantification of radiolabeled magnetic nanoparticles using PET/MRI *in vitro* and *in vivo* for a multi-modality assessment of ^{89}Zr-IONP biodistribution.

Acknowledgments

References

1. Mabray MC, Lillaney P, Sze C-H, et al. In Vitro Capture of Small Ferrous Particles with a Magnetic Filtration Device Designed for Intravascular Use with Intraarterial Chemotherapy: Proof-of-Concept Study. J Vasc Interv Radiol. 2016; 27:426–432e1. [PubMed: 26706187]

2. Kondapavulur S, Cote AM, Neumann KD, et al. Optimization of an endovascular magnetic filter for maximized capture of magnetic nanoparticles. Biomed Microdevices. 2016; 18:109. [PubMed: 27830455]

3. Gurney PT, Hargreaves BA, Nishimura DG. Design and analysis of a practical 3D cones trajectory. Magn Reson Med. 2006; 55:575–582. [PubMed: 16450366]

4. Liu T, Wisnieff C, Lou M, Chen W, Spincemaille P, Wang Y. Nonlinear formulation of the magnetic field to source relationship for robust quantitative susceptibility mapping. Magn Reson Med. 2013; 69:467–476. [PubMed: 22488774]

5. Liu J, Liu T, De Rochefort L, et al. Morphology enabled dipole inversion for quantitative susceptibility mapping using structural consistency between the magnitude image and the susceptibility map. Neuroimage. 2012; 59:2560–2568. [PubMed: 21925276]

6. Liu T, Liu J, De Rochefort L, et al. Morphology enabled dipole inversion (MEDI) from a single-angle acquisition: Comparison with COSMOS in human brain imaging. Magn Reson Med. 2011; 66:777–783. [PubMed: 21465541]

7. de Rochefort L, Liu T, Kressler B, et al. Quantitative susceptibility map reconstruction from MR phase data using bayesian regularization: validation and application to brain imaging. Magn Reson Med. 2010; 63:194–206. [PubMed: 19953507]

8. Lin H, Wei H, He N, et al. Quantitative susceptibility mapping in combination with water-fat separation for simultaneous liver iron and fat fraction quantification. Eur Radiol. 2018

9. Meloni A, Michael Tyszka J, Pepe A, Wood JC. Effect of inversion recovery fat suppression on hepatic R2* quantitation in transfusional siderosis. Am J Roentgenol. 2015; 204:625–629. [PubMed: 25714295]

10. Duda SH, Laniado M, Kopp AF, et al. Superparamagnetic iron oxide: detection of focal liver lesions at high-field-strength MR imaging. J Magn Reson Imaging. 1994; 4:309–314. [PubMed: 8061426]
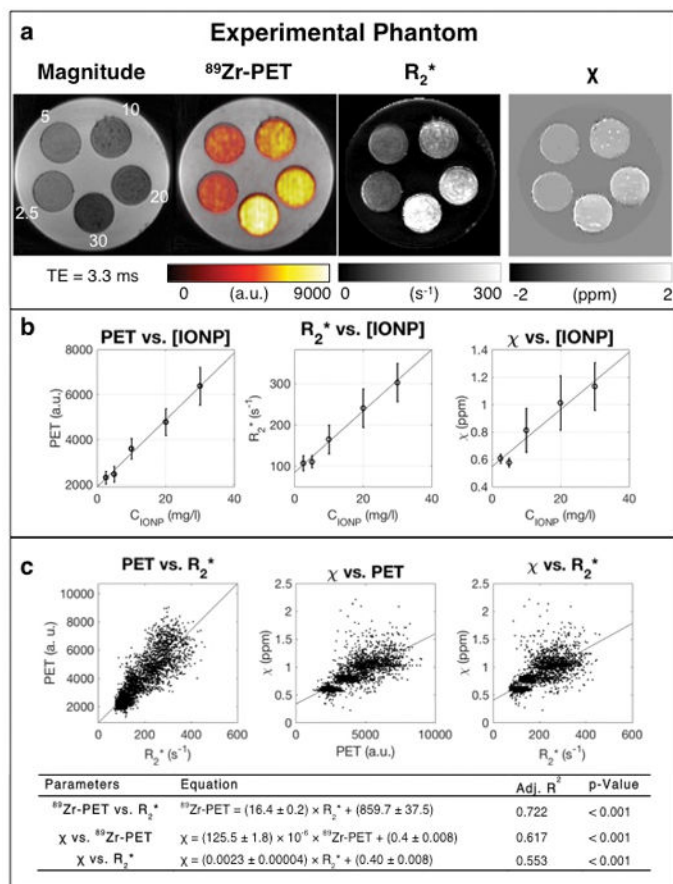
Figure 1. *In vitro* **experiment**

The **a)** magnitude image (second TE = 3.3 ms) annotated with the IONP concentrations (mg/L), ^{89}Zr-PET fused on the magnitude image, R_2* map, and χ map are shown for a single middle slice. **b)** The mean and standard deviation of a manually drawn ROI, in each gel ball are plotted for each parameter, and the means were then fit with a least-squares fit line. **c)** Comparing the parameters with each other, a least squares line was fit between ^{89}Zr-PET and R_2*, χ and ^{89}Zr-PET, and χ and R_2*.
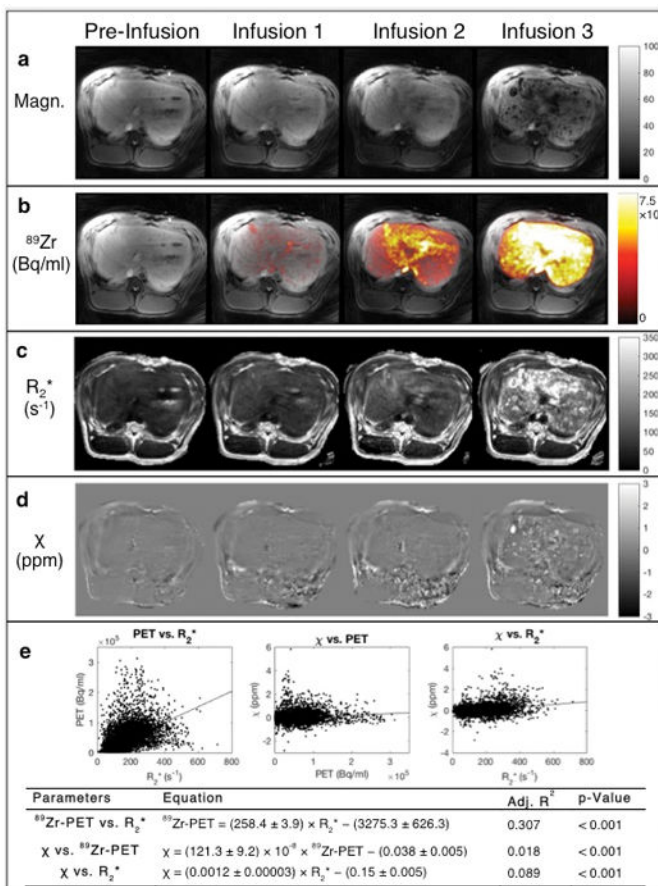
Figure 2. *In vivo* **experiment**
A single middle slice is shown prior to infusion and after each infusion for the **a)** magnitude images (third TE = 3.6 ms), **b)** ^{89}Zr-PET fused on the same magnitude images, **c)** R_2^*, and **d)** χ maps. **e)** Comparing the parameters with each other, a least squares line was fit between ^{89}Zr-PET and R_2^*, χ and ^{89}Zr-PET, and χ and R_2^*.

Table 1

The mean (± standard deviation) of the iron oxide nanoparticle phantom concentrations for each parameter, [89]Zr-PET, R_2*, and χ and the linear regression results for the five mean datapoints versus concentration are reported.

[IONP] (mg/L)	[IONP] (mM)	[89]Zr-PET (a.u.)	R_2* (s^{-1})	χ (ppm)
2.5	0.011	2304.3 ± 272.9	107.1 ± 18.4	0.61 ± 0.03
5	0.022	2453.4 ± 342.5	110.7 ± 14.5	0.58 ± 0.03
10	0.043	3591.1 ± 460.6	164.8 ± 34.7	0.81 ± 0.16
20	0.086	4778.9 ± 597.3	240.5 ± 47.2	1.01 ± 0.20
30	0.130	6376.4 ± 837.6	302.7 ± 46.2	1.13 ± 0.17
Slope (±SE)		149.0 ± 7.5	7.4 ± 0.4	0.021 ± 0.003
Intercept (±SE)		1888.7 ± 127.0	84.9 ± 6.8	0.548 ± 0.048
Adjusted R²		0.990	0.989	0.930
p-value		0.0003	0.0004	0.005

Table 2

The mean (± standard deviation) of the liver ROI before intra-hepatic infusion, and after each infusion, for each parameter, [89]Zr-PET, R_2*, and χ and the linear regression results for the five mean datapoints versus estimated concentration are reported.

IONP (mg/L)	[89]Zr-PET (Bq/ml)	R_2* (s^{-1})	χ (ppm)
Pre-infusion: 0	-	67.6 ± 29.3	−0.033 ± 0.155
Post-infusion 1: 2.5	4,544 ± 2,827	82.7 ± 23.8	−0.042 ± 0.143
Post-infusion 2: 12.5	22,347 ± 13,341	112.9 ± 34.1	−0.027 ± 0.219
Post-infusion 3: 25.0	69,627 ± 42,924	216.2 ± 90.0	0.071 ± 0.528
Slope (±SE)	2929.1 ± 568.5	5.75 ± 0.89	0.0042 ± 0.001
Intercept (±SE)	−6881.2 ± 9210.3	62.3 ± 12.5	−0.050 ± 0.020
Adjusted R^2	0.927	0.931	0.740
p-value	0.122	0.023	0.090